RSC Advances

ROYAL SOCIETY OF CHEMISTRY

www.rsc.org/advances

Cite this: DOI: 10.1039/c0xx00000x

www.rsc.org/xxxxxx

ARTICLE TYPE

Submicron Peanut-Like $MnCO_3$ as an Anode Material for Lithium Ion Batteries

Zhaoxia Cao,[a,b,c] Yanmin Ding,[a,b,c] Jun Zhang,[a,b,c] Qiuxian Wang,[a,b,c] Zhenpu Shi,[a,b,c] Ningning Huo,[a,b,c] Shuting Yang*[a,b,c]

Received (in XXX, XXX) Xth XXXXXXXXX 20XX, Accepted Xth XXXXXXXXX 20XX

DOI reveals: 10.1039/b000000x

Submicron peanut-like $MnCO_3$ is prepared by a facile homogeneous precipitation and delivers better electrochemical performance as an anode material for lithium ion battery. The physical characterization reveals that the peanut-like $MnCO_3$ is composed of irregular nanoparticles, which results a large surface area. As a contrast, square $MnCO_3$ is obtained with structural directing agents. Submicron peanut-like $MnCO_3$ delivers a reversible specific capacity of 700 mA h g^{-1} at 233 mA g^{-1} (1 C = 466 mA g^{-1}) after 140 cycles. The discharge capacities at 46, 93, 233, 466, 932, and 2330 mA g^{-1} are 1047, 1038, 881, 843,750 and 410 mA h g^{-1}, respectively, and a recovery capacity of 1100 mA h g^{-1} after 60 cycles could still be obtained. It also displays a discharge capacity of 618 mA h g^{-1} at high current density of 932 mA g^{-1} after 80 cycles. The advanced performance can be attributed to the unique morphology, facile electron and Li^+ transportations at the electrode/electrolyte interface and self-accommodation of the large volume change during discharge/charge.

Introduction

With the advantages of high energy density, excellent electrochemical performance, no memory effect and long cycling lifetime, lithium ion batteries (LIBs) have been considered as the most attractive energy storage device.[1-2] Among the different anode materials, carbon has been used widely for commercial LIBs ascribed to its good electrochemical and mechanical stability. However, due to its limited theoretical specific capacity (372 mA h g^{-1}), novel anode materials with high performance are highly expected. In various alternatives, metal oxides (SnO_x, NiO, FeO_x, MnO_x, CoO_x) appeared with the advantages of high reversible capacity, high safety and long cyclic performance. Nevertheless, they suffer from the disadvantages of large volume change and rigorous particle aggregation, which result in the collapse of the electrode and capacity attenuation.[3-5] To overcome these problems, the structure of nano-sized metal oxides is optimized with different morphologies[6-8] and importing carbonaceous materials in different combination forms has been reported. For example, the metal oxides/carbon composites of MnO_x/C nanocomposites,[9-11] peapod-like Co_3O_4/C nanocomposites[12] and Fe_3O_4/C nanorods[13] showed higher electrochemical performance than the pure metal oxides. However, the preparation of these materials usually requires complicated synthesis processes which are incompatible for commercial application.

In recent years, metal oxysalts (carbonates, oxalates and oxyhydroxides) which are generally used for preparing oxides, draw researchers' attention due to their unique characteristics of abundance and good electrochemical properties. Different carbonates were reported as the active materials for lithium storage, such as $CoCO_3$,[14] $CdCO_3$, $(BiO)_2CO_3$,[15] and $Mn_{1-x}Co_xCO_3$[16]. However, significant irreversible capacity exists in the initial discharge-charge cycle. $MnCO_3$ was first introduced as an anode material by Aragon for its high capacity, eco-friendliness, and abundant resources, but also for cost-effectiveness and low Li-storage plateau.[17] However, pure $MnCO_3$ also has some disadvantages, such as the poor rate performance and short cycle life.[18]

Herein, we studied the effects of morphology and microstructure of $MnCO_3$ on the electrochemical performance by a liquid phase precipitation. Submicron peanut-like $MnCO_3$ was compounded in a common water solution with fast mixing of original materials. In contrast, the square sample was obtained in water/ethanol system along with cetyl-trimethyl ammonium bromide (CTAB). Compared to the square sample, the peanut-like $MnCO_3$ shows better cycling stability, rate performance and recovery capability. A discharge capacity of 618 mA h g^{-1} is obtained at a high current density of 932 mA g^{-1} after 80 cycles. The advanced performance are ascribed to the unique morphology, facile electron and Li^+ transportations at the electrode/electrolyte interface and self-accommodation of the large volume change during discharge/charge.

Experimental

Materials and methods

The chemicals in our experiments are of analytical grade, and used without any further purification. The $MnCO_3$ samples were obtained by liquid phase precipitation. In the first typical process, 3.71 g of Na_2CO_3 was dissolved in 50 ml distilled water, 0.4 M $MnSO_4$ solution was rapidly added into Na_2CO_3 solution under a magnetic stirring, and a milky white solution appeared immediately. In another synthetic process, 0.1 g of Cetyl-trimethyl ammonium bromide (CTAB) was added into 50 ml 0.35 M NH_4HCO_3 solution, 1.97 g $MnSO_4\cdot H_2O$ was added into the 20 ml water/ethanol mixture (water/ethanol = 1:1 vol%). Then the $MnSO_4$ solution was dropped into NH_4HCO_3 solution under continuous magnetic stirring for 3 h. The resultant were collected by filtration and washed with distilled water and absolute ethanol for several times. Finally, the products were dried at 60 ℃ for 24 h in a vacuum, and severally named as sample SPs, SQs in order.

Materials characterization

The crystalline structure was identified by X-ray powder diffraction (XRD, Bruker AXS D8) analysis with Cu-Kα radiation in the 2θ range from 10° to 80°. The morphology was characterized by scanning electron microscopy (SEM; JSM-6700F). The specific surface area was measured using the Brunauer-Emmet-Teller method (BET, Tristar-II, Micromeritics) with N_2 adsorption and desorption isotherms. The pore size distribution was calculated by the Barrett-Joyner Halenda (BJH) method.

Electrochemical measurements

The electrochemical properties of the $MnCO_3$ powder were evaluated in CR2032 coin cells, which were assembled in a glove box filled with high purity argon gas, both the water and oxygen content levels hold less than 1 ppm. The working electrode is composed of 60wt% active material, 30wt% acetylene black and 10wt% sodium alginate (SA). The lithium metal was used as counter electrode, and micropores polypropylene membrane (Celgard 2400) as separator film. The electrolyte was 1 mol/L $LiPF_6$ dissolved in a mixture of ethylene carbonate/dimethyl carbonate (EC/DMC = 1:1 vol%). Galvanostatic measurement at 233 mA g^{-1} and rate performance from 46 to 2330 mA g^{-1} were tested in the voltage range from 0.01 V to 3.0 V on a LAND Battery test system (CT2001A, Wuhan, China). Cyclic voltammetry (CV) curves were conducted on an electrochemical workstation (CHI660B, Shanghai, China) at a scanning rate of 0.25 mV s^{-1}. Electrochemical impedance spectroscopy (EIS) was performed on an electrochemical workstation (CHI660B, Shanghai, China) over the frequency range of 10^{-1} Hz to 10^5 Hz.

Results and Discussion

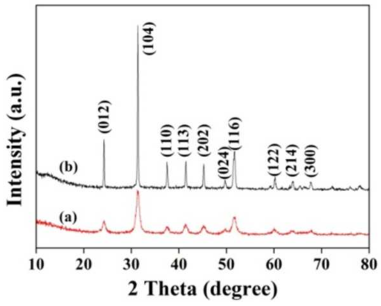

Fig. 1 X-ray diffraction patterns: (a) SPs and (b) SQs.

The phase purity of the two manganese carbonate samples was investigated using XRD. As shown in Fig. 1, all of the diffraction peaks can be indexed to the rhombohedra phase of $MnCO_3$ and no peak of any impurities is detected, indicating the high purity of the samples. However, crystallinities of them are different judging from the peak intensities of their diffraction lines. The SQs display narrower peaks and higher intensities than SPs, corresponding to higher crystallinity.

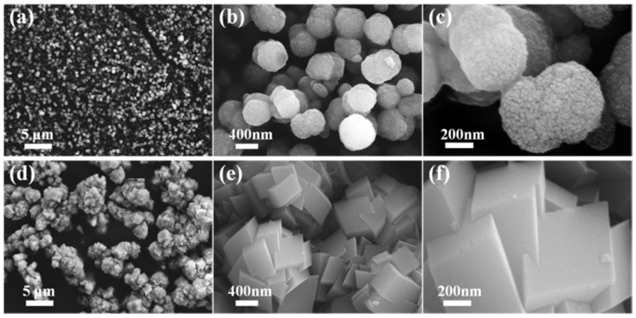

Fig. 2 The SEM images of (a, b, c) SPs, (d, e, f) SQs.

The morphologies of SPs and SQs were studied by SEM. Fig. 2(a-c) shows that SPs present a uniformly peanut-like morphology, with length of ~800 nm and width in the region of 500-600 nm. Rapid mix of reactants results in sharp increase of concentration, and accelerates the supersaturation of the inorganic salts, which facilitates the nucleation rate. The initial crystals prefer to aggregate together, finally form the submicron peanut-like structure. The specific structure assembled from irregular tiny nanoparticles (Fig. 2c) could enhance the $MnCO_3$/electrolyte contact area during the electrochemical reaction.

The square SQs are made of massive interlaced sheets which can be clearly observed in Fig. 2(d-e). The high magnification SEM image (Fig. 2f) further demonstrates this structure arranged in a stagger building block with smooth surface, distinct edges and corners. Moreover, the architecture has side length of 600 nm. Here, due to its steric resistance effect, CTAB facilitates stabilizing the growth of the particles, prevents the further size increase and leads to multifaceted building block with controlled-size and shape.

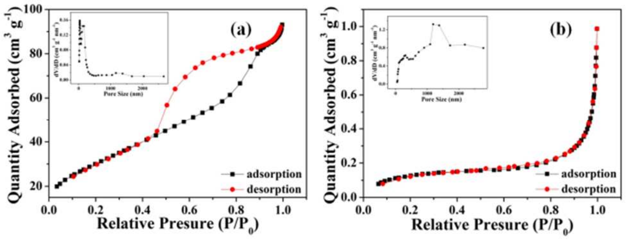

Fig. 3 N_2 adsorption-desorption isotherm curves for (a) SPs and (b) SQs. The insets are the BJH pore size distribution.

To illustrate the surface area and the pore structure, nitrogen sorption-desorption measurements were conducted. Both of them could be classified as type IV with a hysteresis loop as shown in Fig. 3. The SPs exhibit a specific surface area and a pore volume of 110.27 m^2 g^{-1} and 0.144 cm^3 g^{-1}, while the values for SQs are 0.467 m^2 g^{-1} and 0.002 cm^3 g^{-1}. The pore size distributions were reckoned by BJH method as shown inset of Fig. 3. The results imply that the larger surface area and pore volume of SPs could supply more accessible electroactive sites for surface Faradaic reactions, which is beneficial to volume change accommodation and kinetics improvement.

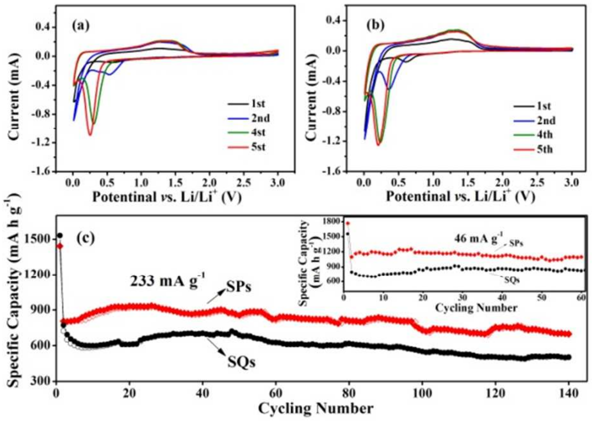

Fig. 4 Cycle voltammogram (CV) profiles of (a) SPs and (b) SQs for the first five cycles at a scan rate of 0.25 mV s^{-1}. (c) Cycling performance at a current density of 233 mA g^{-1} (inset is 46 mA g^{-1}) for two samples.

The lithium storage properties of the two $MnCO_3$ samples were compared via cyclic voltammograms (CV) and galvanostatic discharged-charged performance. Fig. 4(a-b) depicts the cyclic voltammograms curves at a scan rate of 0.25 mV s^{-1} for the first five cycles. In the first cathodic scan, two broad recduction peaks around 0.586 V for SPs and 0.6 V for SQs are observed, which corresponds to the reduction of Mn^{2+} to Mn^0. However, in the following cycles, the main reduction peak around 0.6 V shifts to 0.3 V, mainly relates to the structural change of the strong lithium driven. During the charging process, only one peak appears at 1.29 V for SPs (1.26 V for SQs) which is assigned to the oxidation of Mn and decomposition of Li_2CO_3. It is noteworthy that the broad oxidation peak at 1.29 V (1.26 V) could match with the reduction peak around 0.3 V as a redox. The mechanism of lithium storage in manganese carbonate can be expressed as $MnCO_3 + 2Li \leftrightarrow Li_2CO_3 + Mn$.[18] From the fourth cycle onward, the CV curves become stable and overlap, indicating the good electrochemical reversibility and structural stability.

Fig. 4c shows the cycling performance of two samples. SPs deliver a higher capacity of 1098 mA h g^{-1} at a low current density of 46 mA g^{-1} after 60 cycles (the inset). Furthermore, the reversible capacity of SPs at 233 mA g^{-1} could reach 1420 mA h g^{-1} and 810 mA h g^{-1} in the first and fifth cycle, with an initial coulombic efficiency of 60%. After 140 cycles, the discharge capacity still remains at 700 mA h g^{-1}. As for SQs, the initial coulombic efficiency is 47% and the reversible specific capacity decreases from 1532 mA h g^{-1} to 500 mA h g^{-1} after 140 cycles. These advantages could be attributed to the unique structure of SPs, accommodating the strain induced by the volume change during the electrochemical reaction. Moreover, the large specific surface area could enlarge the contact surface between active materials and electrolyte, reducing the Li^+ diffusion length in the microsphere. For SQs, its instable cubic structure in the architectural is prone to collapse during lithium insertion-extraction process. The aforementioned results indicate that the appropriate morphology of $MnCO_3$ superstructure could be an important factor on the electrochemical performance.

Fig. 5(a, d) shows the discharge-charge plots of 1st, 2nd, 10th, 50th, and 100th cycles for SPs and SQs, respectively. In the first discharging, the plateau at 0.4-0.2 V represents the reaction of $MnCO_3$ and Li into $LiCO_3$ and Mn by Li^+ inserting into the host materials, which contributes to most of the reversible capacity. The slope line from 0.2 V to the cutoff (0.01 V) profits an extra lithium storage capacity of about 400 mA h g^{-1}, which could be ascribed to an interfacial reaction of lithium within the Mn/Li_2CO_3 matrix producing a distinct local charging.[19] During charging, the average Li^+ extraction potential is discovered at around 1.3 V, which is in good agreement with the oxidation peak in CV curves. Indeed, a feature of carbonate-based anode materials is the large irreversible capacity during the first cycles, on account of an interfacial reaction in the discharge process and inactive Li_2CO_3 incomplete decomposition during charge process. The high reactivity of the Mn nanoparticles by the reduction of $MnCO_3$ permits the recombination process.[17] As shown in Fig. 5(a, d), SPs has a lower discharge voltage plateau in the next cycles than SQs, which could be owed to the special structure might relieve polarization.

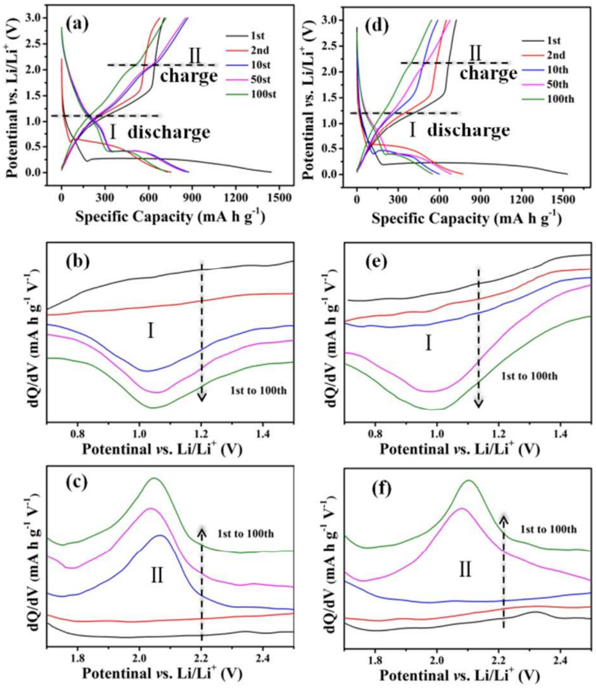

Fig. 5 Discharge-charge curves of (a) SPs and (d) SQs at a current rate of 233 mA g^{-1}, and corresponding differential charge vs. voltage plots of (b, c) SPs and (e, f) SQs at region I (discharge) and region II (charge) in a voltage window of 0.01-3.0 V.

Apart from the aforementioned redox peaks in the CV curves and voltage profiles, two new peaks around 1.05 and 2.05 V appear (Fig. 5b-c and Fig. 5e-f). The anodic peak at 2.05 V is concerned with the re-oxidation of Mn^{2+} to high valence for many Mn-based materials.[20] The cathodic peak at 1.05 V corresponds to the high valence state reduced to Mn^{2+}. Both the peaks are visible after 10 cycles for SPs and their intensities increase gradually, foreboding the existence of multiple high valences. This phenomenon could be also found in SQs after 20 cycles.

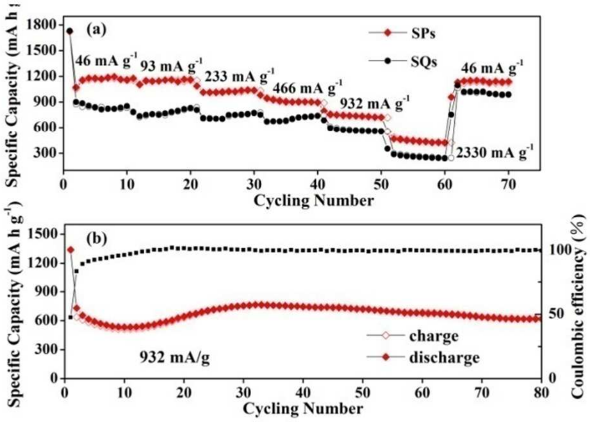

Fig. 6 (a) Rate performance of SPs and SQs electrodes, (b) cycling performance of SPs at a current density of 932 mA g^{-1}.

The same prototype battery was further galvanostatic discharged-charged at increasing current densities of 46, 93, 233, 466, 932, and 2330 mA g^{-1} (Fig. 6a), the corresponding capacities for SPs are 1047, 1038, 881, 843,750 and 410 mA h g^{-1}, respectively, which are higher than that of SQs (875, 831, 769, 743.9, 608 and 315 mA h g^{-1}). AS the current rate is reset to 46 mA g^{-1}, the recovery capacity of SPs increases to 1100 mA h g^{-1}, which is 109% of the initial value. The capacity increase could be ascribed to the inducing reactivation of the materials at high rates. As shown in Fig. 6a, the capacity of SPs is obviously higher than SQs at different current rates. This peanut-like structure could facilitate the electrolyte further permeating into the nanostructure of materials with continuous cycling, which activates the materials piecemeal and then improves the battery performance.

Moreover, the cell was ultimately cycled at a higher current density of 932 mA g^{-1} (Fig. 6b). It slowly decreases from 730 mA h g^{-1} to 618 mA h g^{-1} for SPs after 80 cycles with capacity retention of 85%. The peanut-like $MnCO_3$ with simple synthetic process has higher capacity retention, better rate performance and even superior to other MCO_3, $M_{1-x}M_xCO_3$ and $MnCO_3$/CNTs (M=Mn, Co, Ni, Cd, Zn) composites synthesized by complicated process, as shown in Table 1. This proves that the special structure might relieve the large volume change in lithium insertion-extraction process, and rough porous surface leads to the better electrochemical properties at high rate.[21]

Table 1 Electrochemical properties of MCO_3 anode materials in literatures in comparison to those in this work.

Anode materials	Specific capacity (mA h g^{-1})	Cycles	Rate capacity (mA h g^{-1})	ref
$MnCO_3$ powders	~450	25		17
$(Cd_{1/3}Co_{1/3}Zn_{1/3})CO_3$ nano-flowers	~720 at 60 mA g^{-1}	60	~220 at 680 mA g^{-1}	22
$MnCO_3$ microstructures	~450 at 233 mA g^{-1}	25	~400 at 932 mA g^{-1}	18
$MnCO_3$ submicron	~500 at 466 mA g^{-1}	80		16
$CoCO_3$ urchin -like microspheres	~361 at 100 mA g^{-1}	100	~187 at 2000 mA g^{-1}	23
$MnCO_3$/MWNTs composites	~647 at 100 mA g^{-1}	100	~440 at 1000 mA g^{-1}	24
$Mn_{0.54}Ni_{0.13}Co_{0.13}(CO_3)_{0.8}$	~434 at 250 mA g^{-1}	100	~100 at 2000 mA g^{-1}	25
$MnCO_3$ spheres	~164 at 60 mA g^{-1}	90		26
$MnCO_3$/MWNTs composites	~298 at 128 mA g^{-1}	205		26
peanut-like $MnCO_3$ in this work	~700 at 233mA g^{-1}	140	~410 at 2330 mA g^{-1}	
	~618 at 932mA g^{-1}	80		

Electrochemical impedance spectroscopy (EIS) was carried out to evaluate the electronic conductivity and Li^+ diffusion of materials. The measurements were performed over the frequency range of 10^{-1} to 10^5 Hz after 100 cycles. Fig. 7 shows the corresponding Nyquist plots. All the profiles generally comprise of a depressed semicircle in the high frequency region and a slope line in the low frequency region. The semicircle is associated with the charge transfer impedance of the electrode/electrolyte interface (Rct), and the inclined line is attributed to the solid-state diffusion of Li^+ in the electrode materials (Warburg impedance). From the results, the SPs exert a reduced charge-transfer resistance at high frequencies than SQs testified by the smaller diameter of the semicircle, which confirms large specific surface area could effectively accelerate electron transportation. In the low frequency region, the SPs has a lower diffusion resistance revealed by a straight line along the imaginary axis.

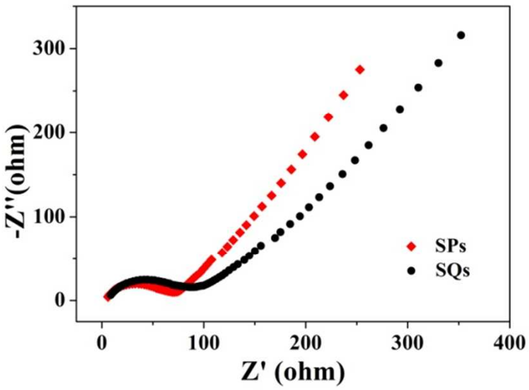

Fig. 7 Nyquist plots of SQs and SPs electrodes in the frequency range from 10^{-1} to 10^5 Hz.

Conclusions

Submicron peanut-like $MnCO_3$ was prepared by a simple homogeneous precipitation without any structural directing agents. Compared with square $MnCO_3$ synthesized in water/ethanol system, the SPs exhibit a high specific capacity of

700 mA h g^{-1} at 233 mA g^{-1} after 140 cycles. Even at 932 mA g^{-1}, the specific capacity also achieves 618 mA h g^{-1} after 80 cycles for SPs. Moreover, it also delivers better rate performance and recovery capability. Based on the electrochemical tests, the unique peanut-like $MnCO_3$ with large surface area and stable structure leads to better transport kinetics during cycling, which enhances electrochemical activity and cycling lifetime.

Acknowledgement

This work was financially supported by National High Technology Research and Development Program of China (863 Program) (2013AA110104) and Research Fund for the Doctoral Program of Henan Normal University (No. 11116).

Notes and references

[a]*School of Chemistry and Chemical Engineering, Henan Normal University, Xinxiang Henan 453007, P. R. China.*
E-mail: shutingyang@foxmail.com; Fax: (+86)-373-3326439; Tel: (+86)-373-3326439
[b]*National and Local Joint Engineering Laboratory of Motive Power and Key Materials，Xinxiang Henan 453007, P. R. China*
[c] *Collaborative Innovation Center of Henan Province for Green Motive Power and Key Materials, Henan Normal University, Xinxiang Henan 453007, P. R. China*

† Electronic Supplementary Information (ESI) available: See DOI: 10.1039/b000000x/

1 M. Li, X. Hou, Y. Sha, J. Wang, S. Hu, X. Liu and Z. Shao, *J Power Sources*, 2014, **248**, 721.
2 L. Wu, Q. Xiao, Z. Li, G. Lei, P. Zhang and L. Wang, *Solid State Ionics*, 2012, **215**, 24.
3 H. S. Lim, B. Y. Jung, Y. K. Sun and K. D. Suh, *Electrochim Acta*, 2012, **75**, 123.
4 B. Wang, J. L. Cheng, Y. P. Wu, D. Wang and D. N. He, *Electrochem Commun*, 2012, **23**, 5.
5 Q. Xiong, J. Tu, Y. Lu, J. Chen, Y. Yu, Y. Qiao, X. Wang and C. Gu, *The Journal of Physical Chemistry C*, 2012, **116**, 6495.
6 M. Gao, P. Zhou, P. Wang, J. Wang, C. Liang, J. Zhang and Y. Liu, *J Alloys Compd*, 2013, **565**, 97.
7 M. Zhang and M. Jia, *J Alloys Compd*, 2013, **551**, 53.
8 T. Li, S. Ni, X. Lv, X. Yang and S. Duan, *J Alloys Compd*, 2013, **553**, 167.
9 S. Wang, Y. Xing, H. Xu and S. Zhang, *ACS Appl Mater Interfaces*, 2014, **6**, 12713.
10 X. Zhang, Z. Xing, L. Wang, Y. Zhu, Q. Li, J. Liang, Y. Yu, T. Huang, K. Tang, Y. Qian and X. Shen, *J Mater Chem*, 2012, **22**, 17864.
11 G. Xu, Y. Xu, J. Fang, F. Fu, H. Sun, L. Huang, S. Yang and S. Sun, *ACS Appl Mater Interfaces*, 2013, **5**, 6316.
12 Y. Wang, H. Zhang, L. Lu, L. P. Stubbs, C. C. Wong, and J. Lin, *ACS Publications*, 2010, **4**, 4753.
13 J. Wang, L. Li, C. Wong, L. Sun, Z. Shen and S. Madhavi, *RSC Adv*, 2013, **3**, 15316.
14 L. Shao, R. Ma, K. Wu, M. Shui, M. Lao, D. Wang, N. Long, Y. Ren and J. Shu, *J Alloys Compd*, 2013, **581**, 602.
15 L. Shao, S. Wang, K. Wu, M. Shui, R. Ma, D. Wang, N. Long, Y. Ren and J. Shu, *Ceram Int*, 2014, **40**, 4623.
16 S. Mirhashemihaghighi, B. Leon, C. Perez Vicente, J. L. Tirado, R. Stoyanova, M. Yoncheva, E. Zhecheva, R. Saez Puche, E. M. Arroyo and J. Romero de Paz, *Inorg Chem*, 2012, **51**, 5554.
17 M. J. Aragón, C. Pérez Vicente and J. L. Tirado, *Electrochem Commun*, 2007, **9**, 1744.
18 M. J. Aragón, B. León, C. Pérez Vicente and J. L. Tirado, *J Power Sources*, 2011, **196**, 2863.
19 J. Shin, D. Samuelis and J. Maier, *Adv Funct Mater*, 2011, **21**, 3464.
20 Y. Sun, X. Hu, W. Luo, F. Xia and Y. Huang, *Adv Funct Mater*, 2013, **23**, 2436.
21 K. Zhong, B. Zhang, S. Luo, W. Wen, H. Li, X. Huang and L. Chen, *J Power Sources*, 2011, **196**, 6802.
22 Y. Sharma, N. Sharma, G. V. S. Rao and B. V. R. Chowdari, *J Mater Chem*, 2009, **19**, 5047.
23 Z. Ding, B. Yao, J. Feng and J. Zhang, *J Mater Chem A*, 2013, **1**, 11200.
24 F. Zhang, R. Zhang, G. Liang, J. Feng, L. Lu and Y. Qian, *Mater Lett*, 2013, **111**, 165.
25 J. Q. Zhao and Y. Wang, *J Mater Chem A*, 2014, **2**, 14947.
26 X. Sun, Y. Xu, P. Ding, G. Chen, X. Zheng, R. Zhang and L. Li, *J Power Sources*, 2014, **255**, 163.